














Small-scale EUV features as the drivers of coronal upflows in the quiet Sun[★]

Conrad Schwanitz^{1,2}, Louise Harra^{2,1}, Cristina H. Mandrini³, Alphonse C. Sterling⁴, Nour E. Raouafi⁵,
Cecilia Mac Cormack¹², David Berghmans⁶, Frédéric Auchère⁷, Krzysztof Barczynski^{1,2}, Regina Aznar Cuadrado⁸,
Éric Buchlin⁷, Emil Kraaikamp⁶, David M. Long^{9,10}, Susanna Parenti⁷, Hardi Peter⁸, Luciano Rodriguez⁶,
Udo Schühle⁸, Phil Smith⁹, Luca Teriaca⁸, Cis Verbeeck⁶, and Andrei N. Zhukov^{6,11}

¹ Institute for Particle Physics and Astrophysics, ETH Zürich, Otto-Stern-Weg 5, 8093 Zurich, Switzerland
e-mail: conradsc@ethz.ch

² Physikalisch Meteorologisches Observatorium Davos, World Radiation Center, Dorf CH, Dorfstrasse 33, 7260 Davos, Switzerland

³ Instituto de Astronomía y Física del espacio (CONICET-UBA), CC. 67, Suc. 28, 1428 Buenos Aires, Argentina

⁴ NASA/Marshall Space Flight Center, 4600 Rideout Rd SW, Bldg 4200, Huntsville, AL 35812-0001, USA

⁵ The Johns Hopkins University Applied Physics Laboratory, 11100 Johns Hopkins Rd, Laurel, MD 20723, USA

⁶ Solar-Terrestrial Centre of Excellence – SIDC, Royal Observatory of Belgium, 1180 Brussels, Belgium

⁷ Université Paris-Saclay, CNRS, Institut d'Astrophysique Spatiale, 91405 Orsay, France

⁸ Max Planck Institute for Solar System Research, Justus-von-Liebig-Weg 3, 37077 Göttingen, Germany

⁹ University College London, Mullard Space Science Laboratory, Holmbury Hill Rd, Dorking RH5 6NT, UK

¹⁰ Astrophysics Research Centre, School of Mathematics and Physics, Queen's University Belfast, University Road, Belfast BT7 1NN, Northern Ireland, UK

¹¹ Skobeltsyn Institute of Nuclear Physics, Moscow State University, 119992 Moscow, Russia

¹² NASA Goddard Space Flight Center, 8800 Greenbelt Rd, Greenbelt, MD 20771, USA

Received 31 January 2023 / Accepted 15 March 2023

ABSTRACT

Context. Coronal upflows in the quiet Sun are seen in a wide range of features, including jets and filament eruptions. The in situ measurements from Parker Solar Probe within ≈ 0.2 au have demonstrated that the solar wind is highly structured, showing abrupt and near-ubiquitous magnetic field reversals (i.e., switchbacks) on different timescales. The source of these structures has been associated with supergranular structures on the solar disc. This raises the question of whether there are additional small coronal features that contribute energy to the corona and produce plasma that potentially feeds into the solar wind.

Aims. During the Solar Orbiter first science perihelion, high-resolution images of the solar corona were recorded using the Extreme Ultraviolet High Resolution Imager (HRI_{EUV}) from the Extreme Ultraviolet Imager (EUI). The Hinode spacecraft was also observing at the same location providing coronal spectroscopic measurements. Combining the two datasets allows us to determine the cause of the weak upflows observed in the quiet Sun and the associated activity.

Methods. We used a multi-spacecraft approach to characterise regions of upflows. The upflows were identified in the Fe XII emission line by the Hinode EUV Imaging Spectrometer (EIS). We then used imaging data from the Atmospheric Imaging Assembly on board the Solar Dynamics Observatory (SDO/AIA) and the High Resolution Imagers (HRI) from EUI on board the Solar Orbiter to identify coronal features and magnetic field data from the SDO Helioseismic and Magnetic Imager (HMI). Interface Region Imaging Spectrograph (IRIS) observations were also used to understand the photospheric and chromospheric driving mechanisms.

Results. We have identified two regions of coronal upflows in the quiet Sun, with respective sizes and lifetimes of (20 Mm², 20 min) and (180 Mm², several hours), which are contrasting dynamic events. Both examples show weak flux cancellation, indicating that the source of the upflows and enhancements is related to the magnetic field changes. The first event, a larger upflow region, shows velocities of up to -8.6 km s⁻¹ at the footpoint of a complex loop structure. We observe several distinct extreme ultraviolet (EUV) features including frequent loop brightenings and plasma blobs travelling along closed coronal loops. The second upflow region has velocities of up to -7.2 km s⁻¹. Within it, a complex EUV feature that lasts for about 20 min can be seen. This main feature has several substructures. During its appearance, a clear mini-filament eruption takes place at its location, before the EUV feature disappears.

Conclusions. Two features, with contrasting properties, show upflows with comparable magnitudes. The first event, a complex loop structure, shares several similarities with active region upflows. The second one, a complex small-scale feature that could not have been well resolved with previous instruments, triggered a cascade of events, including a mini-filament that lead to a measurable upflow. This is remarkable for an EUV feature that many instruments can barely resolve. The complexity of the two events, including small loop brightenings and travelling plasma blobs for the first and EUV small-scale loops and mini-filament for the second one would not have been identifiable as the sources of upflow without an instrument with the spatial resolution of HRI_{EUV} at this distance to the Sun. These results reinforce the importance of the smallest-scale features in the Sun and their potential relevance for and impact on the solar corona and the solar wind.

Key words. Sun: corona – solar wind – Sun: UV radiation

[★] Movies are available at <https://www.aanda.org>

1. Introduction

The solar corona, the Sun's outermost layer, has been the focus of decades-long studies because of the associated challenging phenomena, such as the coronal heating and the acceleration of the solar wind, that shape and impact the whole heliosphere. One potential solution for the heating of the corona was proposed by Parker (1988), who put forward reconnection-driven nanoflares as a potential heating mechanism: small bursts of energy resulting from the reconnection of misaligned magnetic field lines. Parker's proposal requires nanoflares to be frequent. They are, however, so small that they could not be well resolved spatially with previous instruments.

In addition to its high temperature and low density, the solar corona has a range of features, in particular, bright points (e.g., Madjarska 2019), coronal jets (e.g., Raouafi et al. 2016), and extreme ultraviolet (EUV) brightenings (e.g., Harrison 1997; Berghmans et al. 1998). Observations have shown that small EUV intensity bursts are frequently seen in different features, such as active regions (ARs; Testa et al. 2013), coronal loops (Testa et al. 2014), jetlets (Raouafi & Stenborg 2014), and more recently as instability-driven nanojets (Antolin et al. 2021), as well as in blowout jets (Moore et al. 2010, 2013) and coronal rain (Sukarmadji et al. 2022). Small-scale brightenings or UV bursts (e.g., Young et al. 2018) are also present in the transition region (Emslie & Noyes 1978; Widing 1982), chromosphere and photosphere, where they can have relatively high temperatures of up to 100 000 K (Peter et al. 2014). Raouafi et al. (2023b) present a compelling case of ubiquitous jetting, driven by magnetic reconnection, that is present all over the base of the solar corona and is omnipresent throughout the solar cycle. They argue that this form of highly dynamic reconnection and jetting could be the driver of both the fast and the slow solar wind.

One of the main science goals of Solar Orbiter is to understand the sources of solar wind. Since the commissioning of Solar Orbiter EUV Imager (EUI; Rochus et al. 2020), new coronal features have been discovered (see the summary of first perihelion discoveries given by Berghmans et al. 2023). One of the most important discoveries is the observation of the smallest and shortest type of EUV brightening detected so far (Berghmans et al. 2021). They have lifetimes of 10–200 s and lengths of 400–4000 km. Additionally, they reach heights of 1000–5000 km above the photosphere (Zhukov et al. 2021) and might therefore make an important contribution to the transition region-low corona. Summarising their characteristics, they can be seen as an extension of the flare-microflare-nanoflare family (see the summary given by Shibata & Magara 2011). The photospheric magnetic field, seen by the Helioseismic and Magnetic Imager (HMI; Pesnell et al. 2011) on board the Solar Dynamics Observatory (SDO; Pesnell et al. 2011) associated with the EUV High Resolution Imager (HRI_{EUV}) brightenings, shows prominent polarities for most features, and magnetic flux cancellation of a majority-polarity flux by an emerging minority-polarity flux was present for most of them (Panesar et al. 2021). Similar results can be seen for the Polarimetric and Helioseismic Imager (PHI; Solanki et al. 2020) on board Solar Orbiter with which Kahil et al. (2022) were able to find bipolar magnetic structures for 71% of all small EUV brightenings with flux cancellation visible at the footpoints of the brightening loops. Models that cover the upper convection zone up to the corona, which were used to synthesise the coronal emission as seen by HRI_{EUV}, have shown that some of the observed EUV brightenings might be driven by component reconnection (Chen et al. 2021). Tiwari et al. (2022) reported EUV brightenings in a

coronal bright point (CBP) over an emerging flux region. The comparison with magnetohydrodynamic Bifrost simulations (Gudiksen et al. 2011) gave Doppler speeds of about 10 km s⁻¹ for synthetic Fe IX/X images. All these results make magnetic bipoles and magnetic flux cancellation fundamental elements in the formation and triggering of the newly detected EUV brightenings. Even though magnetic reconnection was not clearly observed for these examples, it probably plays an important role since pure flux cancellation would not provide energy and is probably just a byproduct of magnetic reconnection. Examples of small EUV brightenings were seen propagating along loop-like structures. They show behaviours such as bifurcation, merging or reflection at the loop footpoints (Mandal et al. 2021).

Our project focuses on new sources of coronal upflows and extensions to the known ones. Hitherto many coronal features have been known to be sources of plasma upflows. They range from large features such as ARs, to smaller ones, such as CBPs, to transients, such as coronal jets and mini-filaments. Active regions have been identified as the source regions of strong, continuous plasma flows with Doppler velocities of up to 50 km s⁻¹ (Sakao et al. 2007). Redshifted AR coronal plasma in ARs has been associated with closed loops (Del Zanna 2008). The coronal blueshifted plasma, on the other hand, is located in low-intensity regions at the edges of ARs (Del Zanna 2008). Coronal bright points can be seen as downscaled ARs. They are present as small-scale low-coronal loops, which are best visible in EUV and X-ray emissions. The upflows of CBPs are observed by the Hinode/EUV Imaging Spectrometer (EIS; Culhane et al. 2007) in spectroscopic lines covering 6.3×10^5 up to 2×10^6 K with blueshifted Doppler velocities with a magnitude of up to 15 km s⁻¹ (Pérez-Suárez et al. 2008). Orange et al. (2014) observed Doppler shifts both in the transition region, with velocities up to 25 km s⁻¹ and in the corona, with velocities of up to 20 km s⁻¹.

While ARs and CBPs are longer-lasting coronal features, coronal jets are transients. They are prominent features, occurring all over the solar disc. The coronal hole jets can readily be observed due to the lower background emission (Shibata et al. 1992). Kamio et al. (2007) studied jets in the Fe XII spectrum of Hinode/EIS for which a line-of-sight (LOS) Doppler velocity of -30 km s⁻¹ was measured for the jet spire and redshifts of the corresponding coronal hole bright point. Using a double Gaussian fit to the spectral emission line yields jet plasma velocities of up to ≈ 230 – 280 km s⁻¹ (Moreno-Insertis et al. 2008; Madjarska 2011). The first comparisons of observed coronal jets in the quiet Sun by Solar Orbiter's HRI_{EUV} with magnetohydrodynamic Bifrost simulations (Gudiksen et al. 2011) show that filament eruptions occur along with flux cancellation (Panesar et al. 2023). The observed and modelled jets reach velocities of 60 ± 8 km s⁻¹ and 42 ± 20 km s⁻¹, respectively, with lifetimes of 6.5 ± 4.0 min and 9.0 ± 4.0 min (Panesar et al. 2023).

The data from the Parker Solar Probe (PSP) mission (Fox et al. 2016; Raouafi 2022; Raouafi et al. 2023a) have been revealing new insights into the slow solar wind. During the first encounter, PSP observed slow solar wind (36–54 solar radii) originating from a small coronal hole (Bale et al. 2019). The plasma flow is highly structured, displaying a large number of magnetic field reversals, or switchbacks, which are folds of the field lines. These switchbacks are seen over a range of timescales and are separated by intervals of quiet magnetic fields and plasma flow. This might suggest the existence of an impulsive mechanism energising the solar wind and micro-instabilities, which would contribute to the heating. The Alfvénic magnetic

field reversals were found to be associated with supergranulation scales that correspond to their longitudinal separation (Bale et al. 2021; Fargette et al. 2021). This connects them to the diverging magnetic field funnels in the network magnetic field (Bale et al. 2021). The in situ observations of the slow solar wind need an energy source that is small, persistent, and omnipresent. This cannot be satisfied by larger known sources of upflow such as jets or filament eruptions, which are not frequent enough unless the jet-production mechanisms also drive smaller and much more ubiquitous solar features (Sterling & Moore 2020).

Recent work by Schwanitz et al. (2021) has shown that coronal plasma upflows with blueshifted plasma faster than -6 km s^{-1} could be seen from short-lived and weak intensity features down to the resolution limit of the imaging instruments available at the time. Many of the identified features could not be associated with standard features since they only show weak brightenings or faint collimated flows of plasma. While Schwanitz et al. (2021) could only confirm faint soft X-ray sources for some events, five of the features that were more deeply investigated could later be associated with weak intensity X-ray jets by Sterling et al. (2022b). Both studies suggest that the analysis of transient features might be biased towards higher-intensity events and therefore, tend to underestimate the occurrence of small-scale events producing upflows.

Since we have seen in previous work that the identification of small-scale coronal upflow sources has been limited by the spatial resolution of instruments, we aim to find new sources of coronal upflow with the help of the new high-resolution imaging data from HRI_{EUV}. In this paper we explore whether the small structures that are seen by the EUV Imager on board Solar Orbiter are associated with coronal upflows. Section 2 describes the different instruments used for this project and the details of each observation campaign are given. The data processing and alignment of the datasets are described. We then continue by discussing the first upflow region observed on 08 March 2022, in Sect. 3, followed by a discussion of the second upflow region on 17 March 2022, in Sect. 4. We conclude by summarising and discussing our results in Sect. 5.

2. Observation and data processing

We used data from two multi-spacecraft observation campaigns, which were carried out during the first science perihelion of Solar Orbiter in March 2022. The key requirement when selecting the datasets was to have Solar Orbiter HRI_{EUV} data overlapping with Hinode/EIS data that have long enough exposures to provide sufficient signal-to-noise ratios for quiet Sun regions. The first campaign ran on 08 March 2022 between 08:10 and 10:10 UT as the Solar Orbiter Observing Plan (SOOP) ‘R_BOTH_HRES_MCAD_Bright-Points’ and the second one as SOOP ‘L_SMALL_HRES_HCAD_Slow-Wind-Connection’ on 17 March 2022 between 09:47 and 10:47 UT. The characteristics of the instruments participating in these campaigns are discussed in the following sections.

2.1. Solar Dynamics Observatory (SDO): AIA and HMI

The Atmospheric Imaging Assembly (AIA; Lemen et al. 2011) continuously provides full-disc observations in ten different channels from the photosphere up to the corona, covering temperatures from roughly 5000 K up to 20 million K. We use level 1.5 data with a 12 s cadence from the Joint Science Operations Center (JSOC). The data were processed by scaling the image

to $0.6 \text{ arcsec pixel}^{-1}$ and extracting sub-images that cover the region observed by the other instruments.

The second SDO instrument used is HMI (Scherrer et al. 2012), which measures the photospheric magnetic field. We focus our analysis on the LOS magnetograms. They are provided at a 45 s cadence and require only a de-rotation of 180° for processing. For any quantitative analysis, we neglect data with absolute values below 10 G, which is considered the noise level (Liu et al. 2012).

2.2. Solar Orbiter Extreme Ultraviolet Imager (EUI)

The true value of the observation campaign lies in the data from Solar Orbiter (Müller et al. 2020) taken during its first science perihelion. The data used in this project comes from the Extreme Ultraviolet Imager (EUI; Rochus et al. 2020). It consists of three instruments: a dual-band Full Sun Imager (FSI), which provides 174 and 304 Å EUV images and two High Resolution Imagers (HRI), which measure emission in the Lyman- α -line of hydrogen at 1216 Å and EUV at 174 Å. HRI_{EUV} mostly measures the Fe IX 171.1 Å, Fe X 174.5 Å and Fe X 177.2 Å emission lines, which are emitted around 800 000–1 000 000 K. We focus our analysis on the HRIs, which provide images with 2048×2048 pixels and a field-of-view of roughly $1024'' \times 1024''$. The HRI_{EUV} instrument has a two-pixel resolution of approximately $1''$. The HRI_{Ly α} has a resolution of approximately $3''$, which worsened during perihelion and recovered to the previous values after it (Berghmans et al. 2023, this issue). The EUI data files used in this paper were taken from the SoLO/EUI Data Release 5.0 (Mampaey et al. 2022).

The first observation was carried out when Solar Orbiter was at a distance to the Sun of 0.48 au. The separation of Solar Orbiter and the Earth in heliographic longitude is 1.85° . This results in a pixel size of $(172 \text{ km})^2$ and a travel time difference of 253 s for emission from the Sun to Solar Orbiter compared with radiation to the Earth. This travel time difference was taken into account for every step of the analysis. All times of EUI in the text and in plots are shifted to match those of an Earth-based observer. The HRI instruments were operated for the first observation in a low-cadence mode with one image per minute and an exposure time of 2.8 s for HRI_{EUV} and 3 s for HRI_{Ly α} .

The second observation was taken close to the perihelion at a distance of 0.38 au and a separation between the spacecraft and the Earth of 27.5° . This results in a travel time from the Sun to the spacecraft of 187 s. The corresponding pixel size is $(134 \text{ km})^2$. The HRI instruments were operated for the second observation in a high-cadence mode with one image every 5 s. Each image was exposed for 2.8 s by HRI_{EUV} and 3 s by HRI_{Ly α} .

The level 2 data were used, which is the calibrated science data. The biggest challenge lies in the alignment of the Solar Orbiter data to other datasets due to the different locations of the spacecraft. We made use of the FITS keywords for a first alignment. In a second step, we re-projected Solar Orbiter maps to an Earth-based helioprojective coordinate system. This allowed us to cross-correlate EUI/HRI maps with SDO/AIA 171 Å filter maps, to calculate their offsets. To do so, the resolution of EUI was reduced for the alignment to match that of SDO/AIA. The analyses are done with the full resolution of EUI/HRI. All EUI maps were then shifted to the SDO/AIA frame. This leads to reasonable results with a precision of about one AIA pixel. However, the two instruments have different viewing angles and temperature response functions, which leads to re-projection effects and intensity variations respectively. Hitherto, no general

correction of those two effects is available. Therefore, optical differences are to be expected.

2.3. Hinode EUV Imaging Spectrometer (EIS)

The EIS instrument on board Hinode (Culhane et al. 2007) mission was launched in 2006. The sensitivity of its short wavelength channels peaks close to the Fe XII 195.12 Å emission line, which makes it the most prominent line in most observations. It represents a coronal temperature of $\log T_{\max} = 6.1$. This makes it the best choice for observations of quiet regions in the solar corona and that is why we focus our analysis on it.

The first observation was from the Hinode Operation Plan (HOP) 430 “Bright Point study with Solar Orbiter”, which uses a 2'' slit to raster at 83 different positions with 45 s exposure time for each slit position. The resulting raster covers $497'' \times 512''$ and takes 1 h 8 min. We focus on the first raster at 07:51 UT from the campaign since the following rasters are highly affected by data loss.

The second observation was conducted on 17 March 2022 and run as HOP 434. It consists of two consecutive rasters, which were run at 08:16 UT and 09:52 UT. They cover a field-of-view of $246'' \times 521''$ and have a duration of 1 h 7 min 30 s. Each raster has 62 pointings with an exposure time of 1 min and a step size of 4''. We focus our analysis on the second raster from this campaign.

All rasters are processed with the Python environment EIS Python Analysis Code (eispac). The spectral data are further processed by using a single Gaussian fit for the Fe XII line at 195.12 Å within a fitting window for the centroid from 195.08 Å to 195.16 Å to compute intensities and Doppler velocities. The velocities are calculated with respect to the theoretical line at rest and the derived Doppler maps are corrected for orbital effects. This includes correcting the orbital effect of the spacecraft’s temperature variation. This effect is corrected by setting the median Doppler velocity of each column to zero. A double Gaussian approach to allow for the line blending of the weaker Fe XII line at 195.18 Å (Young et al. 2009) did not converge due to the small intensities in the quiet Sun.

To make the Hinode/EIS rasters comparable with other datasets, we aligned them with SDO/AIA 193 Å data. It is the closest available AIA filter to the Fe XII emission line. We start by shifting the data manually. To improve the alignment, we reduce the spatial resolution of SDO/AIA to match that one from Hinode/EIS. This is done to use cross-correlation to determine the best alignment between the two datasets. The derived offset is then applied to the Hinode/EIS rasters.

2.4. The Interface Region Imaging Spectrograph (IRIS)

We also used data from the Interface Region Imaging Spectrograph (IRIS; De Pontieu et al. 2014), which focuses on chromospheric and transition region emission. Both observing campaigns were supported by a coordinated IRIS observation.

The campaign on 08 March 2022 used a very large dense 320-step raster with a field-of-view of $167'' \times 175''$. In addition to the spectral data in the near UV and far UV wavelength range, slit-jaw-images (SJIs) are available for C II 1330 Å, Si IV 1400 Å, Mg II k 2796 Å, and the Mg II wing 2830 Å, respectively. These lines cover temperatures from the upper photosphere up to the lower transition region.

The second campaign on 17 March 2022 used a very large dense 4-step raster with a field-of-view of $166'' \times 175''$.

Slit-jaw images were taken only for the Si IV 1400 Å emission line, formed at 80 000 K in the lower transition region. Unfortunately, our selected feature falls outside of the field-of-view of the IRIS observation.

For the analysis of the photosphere, chromosphere and transition region data, we use IRIS SJIs. They are provided as level 2 science data by the Heliophysics Events Knowledgebase (HEK).

To align the IRIS data with other datasets, we made use of the SDO/AIA 1600 Å waveband, which is composed of photospheric and transition region emissions. We used the IRIS SJI data from the 1400 Å waveband, which represents the low transition region. As before, the first step was to reduce the spatial resolution from IRIS to match that from SDO/AIA. Then we took $100'' \times 100''$ sub-frames of the regions of interest and aligned them using cross-correlation. The offset was then applied to the IRIS SJIs.

2.5. Approach

We started the analysis of each event with the Hinode/EIS Doppler velocity maps. Within these maps, we looked for small regions of coronal upflow stronger than -6 km s^{-1} , which was found to be a reasonable level for small features in Schwanitz et al. (2021). We manually selected regions due to their strength and isolation from other blueshifted regions. Blueshifts are seen all over the corona. For our further analysis, we excluded events that are known sources of strong upflows such as ARs or regions of obvious coronal jets. In the second step, we add EUV imaging data to the Doppler maps to visualise the source regions and identify potential small-scale features that can be associated with the upflows. In the last step, we use photospheric magnetic field data and sub-coronal imaging data to better understand the driving mechanisms of the observed EUV features. This approach helps us identify upflow regions without being biased towards easy-to-see features and potentially identify new sources of coronal upflow. In the next sections, we discuss our two example datasets separately.

3. The upflow region on 08 March 2022

We first describe the 08 March 2022 event since it is less complex. It is located at $[-83'', 90'']$ at around 08:36 UT and consists of two almost perpendicular loop systems (see Fig. 1). Upflows are seen along both loop structures and towards regions of less intensity. We focus our analysis on the strongest upflows, which are seen on the northern end of the longer loop structure, which extends towards the south-east. It is highlighted by a blue contour of -6 km s^{-1} . South of this upflow region a faint elongated brightening is seen in SDO/AIA 193 Å at $[-80'', 87'']$ pointing directly southwards. This structure might indicate another loop system with a length of about 20–30''.

The photospheric magnetic field (Fig. 2) shows that both the north-eastward and south-eastward orientated coronal loop structures have an underlying positive flux at the end where we observe the strongest upflows, highlighted by the blue contour. The lifetime of the whole structure is about 1.5 days. The shorter one towards the north-east is connected to stronger compact negative polarities at around $[-125'', 125'']$, while the longer one is bound to stronger negative polarities in the south-east (not shown in Fig. 2, see online movie 1). Additional small, negative, less complex fluxes are present directly south of the positive polarity at $[-90'', 55'']$, which seem to be part of a medium size loop structure and can be seen in AIA 171 Å. Besides the long

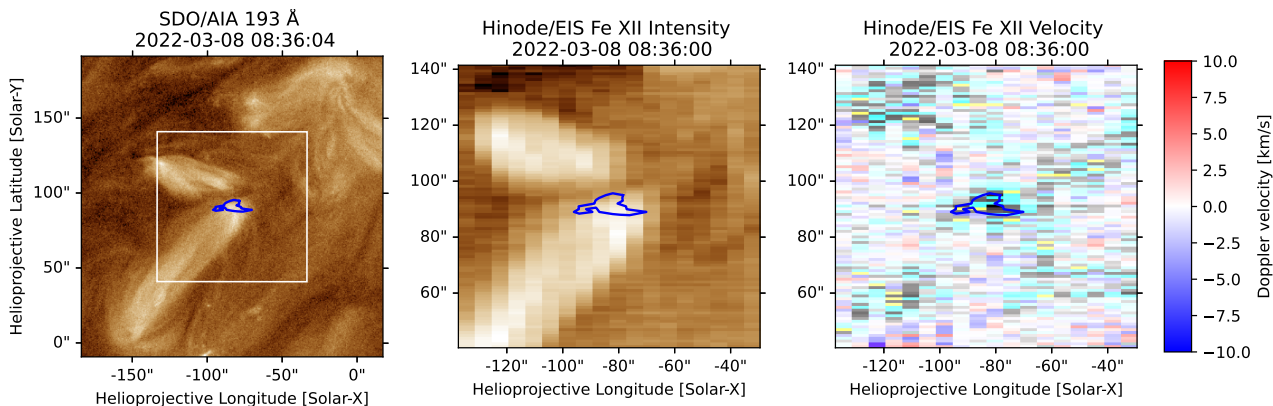


Fig. 1. Coronal emissions and Doppler shifts seen in Fe XII. Left panel: region of interest showing two long loop structures, which are almost perpendicular to each other. The focus is on the southern one since it shows the stronger upflows. It is twice as long as the other one. Central panel: intensity of the Hinode/EIS Fe XII line, the southern loop starting at around $[-80'', 90'']$, where it is the brightest. Right panel: Doppler velocity from the Fe XII line, showing that the starting point of the southern loop is a region of strong upflows. We define the upflow region with a -6 km s^{-1} contour, which is drawn in blue.

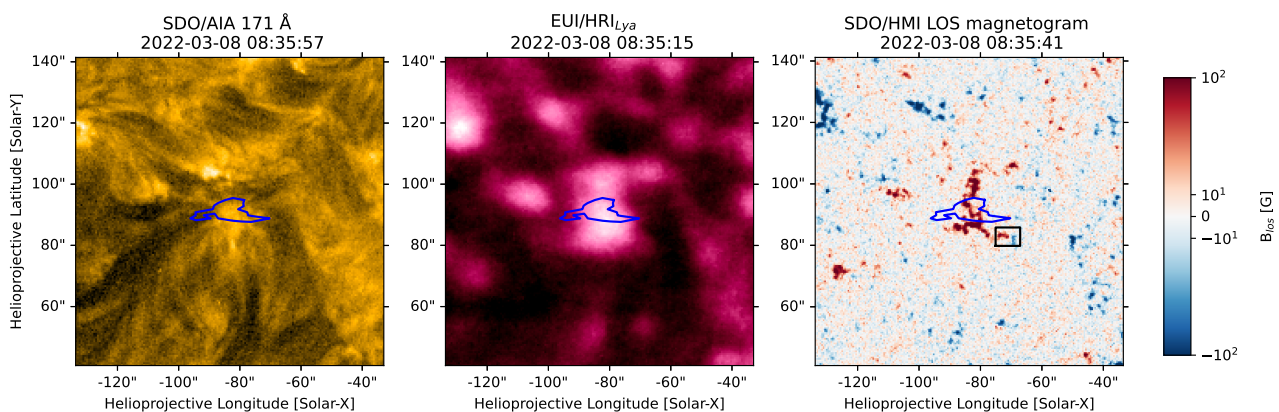


Fig. 2. Coronal emissions in Fe IX, the chromospheric network in Ly- α , and the photospheric LOS magnetic field. Left panel: coronal structures seen in 171 Å by SDO/AIA, showing a complex loop system. It is divided by loops, which are either northward or southward directed. The southward loops seem to consist of medium-sized coronal structures, which are directed purely southwards, and longer ones, which are pointing towards the south-east. Central panel: upflow region located on a bright structure of the chromospheric network, measured by HRI_{Ly α} . Right panel: photospheric magnetic field revealing a strong positive polarity beneath the coronal upflow. It reaches values above 100 G. A black box in the south-west of the structure shows a region where we measure flux cancellation.

loop structures anchored to the opposite negative polarity, we can observe flux cancellation at two sides of the positive polarity. The first one occurs in the north-west $[-75'', 110'']$ (see [online movie 1](#)) and the second one in the South-West part $[-75'', 85'']$ (see [online movie 1](#) and Fig. 3). It is worth noting that the loop systems south of the upflow region look rather different in the 193 Å (Fig. 1) and in the 171 Å (Fig. 2) waveband. While we only see the long loop in the former, we have several shorter ones in the latter. Taking into account that the 171 Å waveband contains spectral lines emitted at slightly cooler temperatures of around 600 000 K, it is not purely coronal, but also contains transition region emissions. Therefore, we conclude that the purely southward-directed loops are lying beneath the south-eastwards-directed loops. This will be later on even more supported when we compare it with the HRI_{EUUV} data. The chromospheric observation by HRI_{Ly α} shows that the HMI polarity is seen under the chromospheric network, which coincides well with its lifetime of 1.5 days, which is comparable to the network turnover time.

This particular region was partly covered by a coordinated IRIS observation. The positive polarity seen in HMI is present as brightenings in all four SJI wavebands. However, it was unfortu-

nately not covered by the slit. As seen in Fig. 4, the same structure, which can be seen as a photospheric positive polarity in HMI, extends throughout the chromosphere and transition region as a brightening. Those structures trace the chromospheric network and locate our upflow feature on the network. Its shape is similar throughout the different heights. Furthermore, individual brightenings, which are spatially separated from the main structure, can be backmapped to small patches of negative and positive polarity in HMI. An example, best seen in the 1330 C II waveband, is at $[-70'', 82'']$, which corresponds to the negative polarity highlighted by a black box in Fig. 2 for which we have measured flux cancellation. Comparing the chromospheric data in the 1330 C II waveband, we can clearly see that the observed structure lies on the chromospheric network.

The HRI_{EUUV} observation of the southern loop complex in Fig. 5 reveals a variety of interesting features. The first thing to notice is that the main bright structure associated with the coronal upflow is observed over the whole observation time. The bright region does not change drastically in its general shape and size. It is the footprint of three different loop systems, a long loop system towards the south-east, which we have already seen

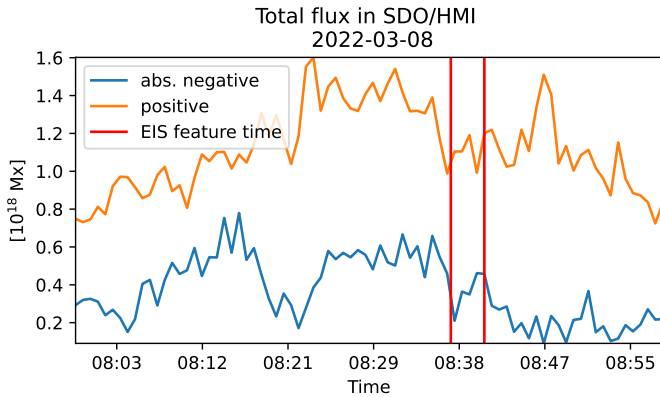


Fig. 3. Total flux within the region of the strongest upflow and its vicinity (highlighted by a black box in Fig. 2) starting with a strong positive polarity patch at the south-west edge and weak negative polarity at 07:59 UT. We see three time periods where the total negative flux gets stronger by more than a factor of two (08:05 UT, 08:20 UT, 08:37 UT) and then gets cancelled out by the approaching positive polarity (08:15 UT, 08:32 UT, 08:40 UT). The third such time period coincides with the time when Hinode/EIS observes the upflow (highlighted by red lines). Towards the end, the negative polarity mostly disappears and only smaller remnants are left.

in SDO/AIA 193 Å. A medium-sized loop system, which is the confirmation of an additional loop system, which we defined in SDO/AIA 193 Å and a system of short loops, which is otherwise only visible in SDO/AIA 171 Å.

To support our identification of the just described three-loop systems and understand their relation to the outflow region overlaying the HMI positive polarity, we modelled the magnetic field using a force-free approach and taken as boundary condition the HMI magnetogram closest in time to a HRI_{EUV} image at around 08:25 UT. The model, methodology to derive its free parameters, and its limitations have been described elsewhere (see Mandrini et al. 2015; Harra et al. 2021, and references therein). Figure 6 shows an overlay of the field lines computed from the model on the HRI_{EUV} image, compared to the three-loop systems seen in the top-left panel of Fig. 5. Three sets of pink field lines would represent the longer, medium-sized, and shorter loops in that panel. All of them are anchored in the strong upflow region and have opposite footpoints in south-eastern and southern negative HMI polarities. The projected shape of the longer field lines does not closely match the shape of the longer EUV loops, which we attribute to a limitation of the force-free model. The sets of field lines in Fig. 6 are drawn so that they can be clearly seen without any overlap; we notice that the computed longer lines reach a maximum height larger than the nearby shorter ones to the east. We are also showing sets of field lines drawn in light blue for context; these lines match the shape of HRI_{EUV} loops not related to the upflow region on the positive HMI polarity.

Frequent small-scale activities are seen at the footpoints of the medium-size and short loop systems, identified in Fig. 5, and within the loops themselves. We notice several small brightenings that are highlighted by red arrows in the lower-left panel of Fig. 5, which appear close to the origin of the loops. The corresponding online movie 2 shows that they originate from the brightest region and fade out while moving along the loop structures. Similar brightenings at the loop bases in an AR have recently been observed by EUV (Berghmans et al. 2023). In our case, they are mostly present towards the south and south-east. Secondly, loop brightenings are seen within the loops. They do

not travel along the loops, but rather stay in the same position. Similar brightenings have previously been associated with braided loop structures. Then we see small bright patches that originate at the footpoint of the loop and travel along the loop structure, where they either fade out or cause a strong secondary brightening at the end. We measured and displayed these brightenings in Fig. 7. An example of a travelling plasma blob is seen at 09:49 UT, which travels for a distance of about 50'' with a speed of 33 km s⁻¹. An example of a brightening within the loop is seen at 10:01 UT at a distance of about 45'' from the footpoint, which corresponds roughly to its vertex point. Those small features have not been seen before for such small loop systems and due to their frequency they eventually contribute to the measured plasma upflow.

The upflow region on 08 March 2022 is located at the footpoint of a complex loop structure. We see at least three separate loop systems that connect to different footpoints and have different lengths. Only one loop is present in SDO/AIA 193 Å, while the other ones are present in SDO/AIA 171 Å. The underlying photospheric magnetic field reveals a strong positive polarity from which the loops originate and connect to several smaller patches of negative polarity. At the edges of the big positive polarity, we observe flux cancellation of neighbouring negative polarities. The HRI_{EUV} data shows strong activity within and along the loops. The loop system, which originates at the region of flux cancellation, shows high activity in the form of loop brightenings or plasma blobs travelling along the loop. The observed footpoint region of the different loops has a size comparable to a large CBP, while the measured upflow velocities are about half of those of CBP (for example 15 km s⁻¹ in Pérez-Suárez et al. 2008). The velocities of the travelling plasma blobs exceed the measured upflow speeds and are more comparable to Doppler flows measured in ARs. Similar to AR flows, we measure the strongest upflows at the footpoint or edges of the loop system. The source of the observed upflow is probably a combination of the several small EUV features, that we observe mostly at the footpoints of the loops, where the strongest upflows are measured.

4. The upflow region on 17 March 2022

The 17 March 2022 event is more complex than the first event since it consists of multiple, linked small-scale features. We defined the feature in the Doppler velocity map (see Fig. 8) of the Fe XII line as a region of enhanced blueshifts that is surrounded by mostly downflows. Its location in helioprojective coordinates is at $x = 120''$ and $y = -725''$ which corresponds to an event time of 10:29 UT. The upflow region has a maximum Doppler velocity of -7.2 km s⁻¹. The preceding raster does not show upflows within this region, but due to the lack of a following raster, the exact duration of the upflow cannot be determined. The intensity in the upflow region is slightly increased within the low-intensity region in contrast to the pixels directly outside of the outflow (see the central panel in Fig. 8). The upflow extends from the south-east to the north-west and shows a small elliptical feature in intensity, which does not have any substructure.

We initially combine the Hinode/EIS data with SDO/AIA in order to be able to compare the results to Schwanitz et al. (2021). The waveband at 193 Å is the closest in temperature to the Fe XII emission line (see Fig. 8). In the associated online movie 3 of this waveband, a small bright point appears at 10:12 UT and persists until about 10:37 UT. It does not show any eruptions or jets. Its peak intensity is reached at 10:28 UT.

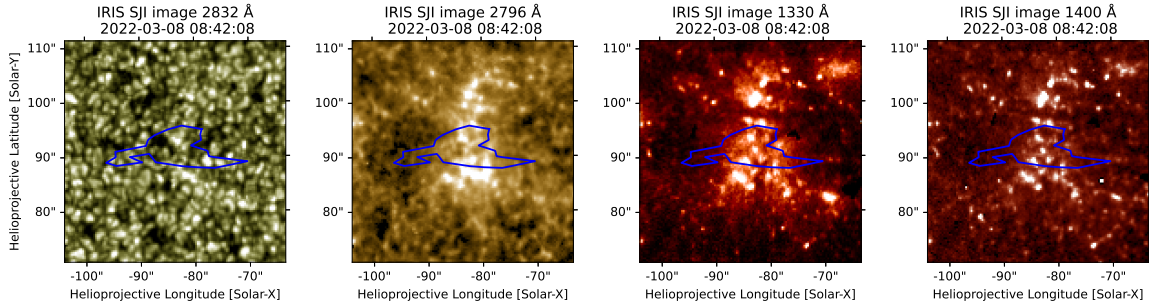


Fig. 4. SJIs from IRIS showing a bright structure within the upper chromosphere (2796 Å and 1330 Å) and the upper transition region (1400 Å). The upflow region falls on the chromospheric network. No clear structure can be seen in the upper photosphere (2832 Å).

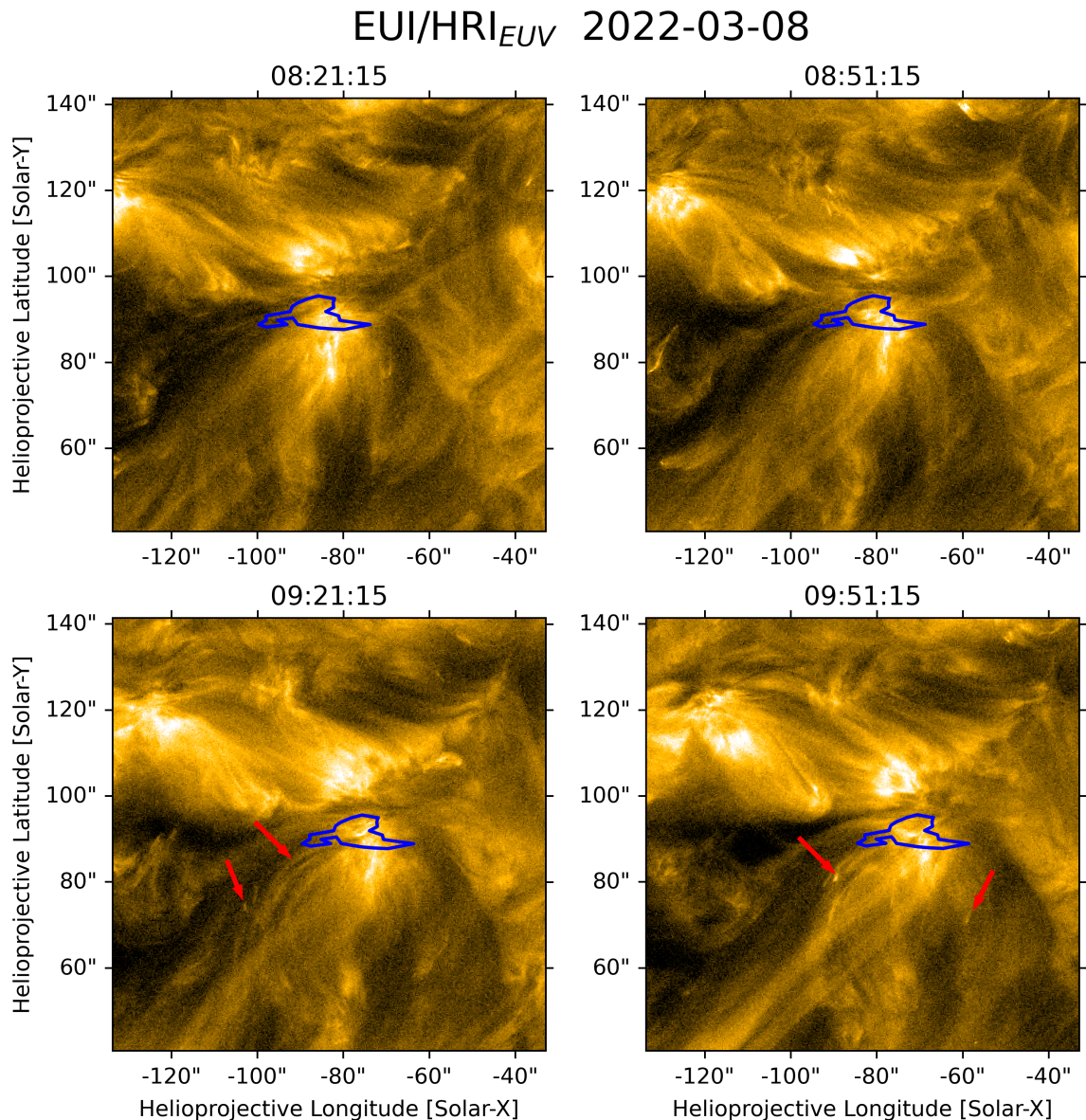


Fig. 5. Observation of HRI_{EUV} showing that the large bright footpoint region of the different loop systems, where we observe the strongest upflows, is rather stable over time. All plots are re-projected to an Earth-based helioprojective coordinate system. Top-left panel: three different loop systems. The left one corresponds to the longer loops which are clearly visible in AIA 193 Å. The central one connects to HMI polarities at $[-90'', 50'']$ and the right one, which is the shortest connects to negative polarities at $[-70'', 55'']$. Top-right panel: structure and loop systems remain stable over a time period of 30 min. Bottom-left panel: brightenings at the footpoints of the central loop system are highlighted, such as isolated brightenings within individual loops. Bottom-right panel: loop brightenings and travelling brightenings flow along the medium-sized central loops and the shorter loops in the eastern system.

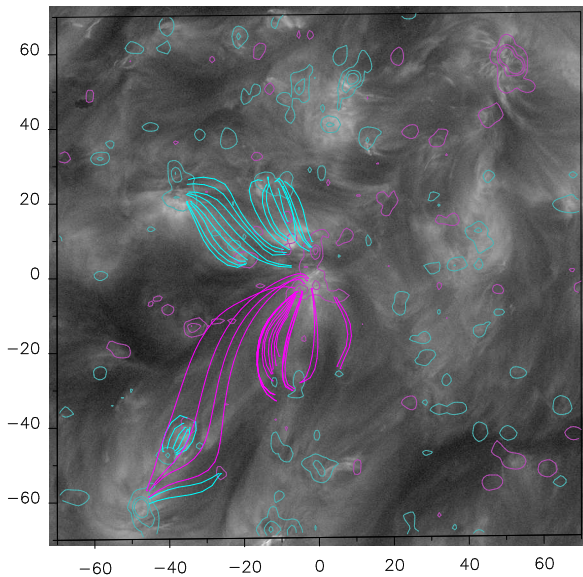


Fig. 6. Magnetic field model of the region surrounding the positive HMI polarity where the strong upflows are located. The model is overlaid on the HRI_{EUV} image at around 08:25 UT, shown in grey scale. Computed field lines (in pink) matching the global shape of the observed loops have been added for those anchored in the upflowing plasma region (see the comments in the text). Other sets of loops are shown in light blue for context. The axes in the panel are in units of Mm, with the origin in the region of interest. The isocontours of the LOS field correspond to ± 10 , ± 50 , and ± 100 G; pink shows positive values and blue negative values.

Figure 9 shows the AIA 171 Å waveband data, the chromospheric data from $\text{HRI}_{\text{Ly}\alpha}$ and the magnetic field. A similar brightening as in the 193 Å waveband is seen from 10:12 UT to 10:36 UT in the 171 Å waveband. It seems to be part of a bigger, triangular-shaped, diffuse structure that extends well out of the blueshifted contour. The bigger structure reaches in solar- X from 105'' to around 130'' and from $-745''$ to $-725''$ in solar- Y . Following this brightening the [online](#) movie 4 shows a mini-filament erupting from the location of the brightening beginning between about 10:10 and 10:15 UT. It travels for about 20'' southwards until it is no longer visible in intensity (compare Fig. 10). It reaches a maximum length of about 10'' perpendicular to its directional movement. This is likely a ‘confined’ mini-filament eruption, whereby the mini-filament does not escape the base region. Such erupting mini-filaments can affect higher-altitude magnetic structures, sometimes producing jets (Sterling et al. 2022a). The mini-filament eruption triggers a quasi-circular front of bright material, which can be seen from the north-east up to the south-west. Following this eruptive event, we can see further brightenings at 10:37 UT at $[-730'', 130'']$. This might suggest that additional hotter plasma has also been expelled towards the north. Over the whole triangular-shaped structure, smaller changes are seen, which indicate reconnection and restructuring of the local field. The mini-filament eruption was a small-scale event, and it was too weak to make a strong signature in AIA filters other than 171 and 193, so we can only speculate as to how this eruption, which was restricted to a compact portion of the larger region that showed the EIS outflows, could have made those much larger outflows. One possibility is that the mini-filament eruption triggered the eruption of the surrounding magnetic field that carried the quasi-circular front of bright material and that this triggered an even larger eruption that

led to the EIS outflows over the larger region. Another possibility is that the expelled plasma forming the quasi-circular brightening moved out along weak open magnetic fields threading the EIS outflow region, this idea will be discussed later in our magnetic field extrapolations. Although these ideas of how the compact mini-filament eruption made the larger-area EIS outflows are speculative, we do note that mini-filament eruptions do appear to be scaled-down large-scale eruptions (Sterling et al. 2015), and large-scale filament eruptions are capable of triggering eruptions covering a much larger area than just the localised location where the filament erupted (Sahu et al. 2022).

Using data from $\text{HRI}_{\text{Ly}\alpha}$, we determine that the upflow feature is located at the boundary of the chromospheric network (see Fig. 9).

The underlying photospheric magnetic field shows several opposite polarities around the upflow region. Most prominent is a positive polarity at $[-733'', 122'']$ surrounded by negative polarities, all of which are rooted outside of our upflow region. These might form a system of magnetic loops, which we see as the triangular-shaped structure in SDO/AIA. Within the upflow region we see small flux cancellation, seen in Fig. 11 and [online](#) movie 5. It was measured within a region at the south-east of the upflow region (compare with Fig. 9). The black box outlining the magnetic flux is not centred on the polarities since the polarities move westwards over time. The configuration starts with a stronger positive and weaker negative polarity. The positive gets annihilated by the emerging negative, which exceeds the positive one at around 10:04 UT. The flux cancellation lasts until about 10:20 UT. After this, the positive flux emerges again about 30 min later.

There are some changes seen in the magnetic field data at the south-eastern edge of the upflow region. However, from the AIA data, it is not clear how those changes affect the coronal upflows. We then analysed the HRI_{EUV} data to determine the influence of smaller-scale features.

Up to this point, this upflow feature would have been classified as an unresolved small-scale brightening accompanied by a mini-filament eruption. With the help of the new EUV/HRI data, we were able to determine a much more detailed understanding of the EUV structure: the upflow region in the HRI_{EUV} starts without any distinct features. The HRI_{EUV} [online](#) movie 6 shows within the first 13 min (09:52–10:05 UT), four small brightenings, which follow the characteristics described by Berghmans et al. (2021). They have both dot- and loop-like structures, lifetimes from 2 to 5 min and sizes of around 0.3–1 Mm^2 . This is comparable to the brightenings found by Berghmans et al. (2021) with lifetimes of 10–200 s and lengths of 400–4000 km. However, they are spatially distributed and only one of them falls into the region, where we observe the upflow about 10 min later. This does not allow us to make a direct connection to any succeeding feature and the plasma upflow. A more prominent feature arises at the south-east of the upflow $[110'', -730'']$ at 10:08 UT, which consists of two parallel loops, which are present for about 5 min. At the location of the previous brightening, a second and much stronger feature appears at 10:17 UT (Fig. 12, top-left panel) and lasts for about 20 min. The feature shows clear substructures, which change over time. Its shape is from a single loop to a cross-like structure (Fig. 12, top-right panel) with four extended spines. The maximum area is 25 Mm^2 . After the disappearance of the feature, two further small brightenings appear. Besides those features within the observed upflow region, a structure of two parallel loops appears in the north-west end of the upflow region $[128'', -712'']$ at 10:21 UT (Fig. 12, top-right panel) and exists for about 6 min.

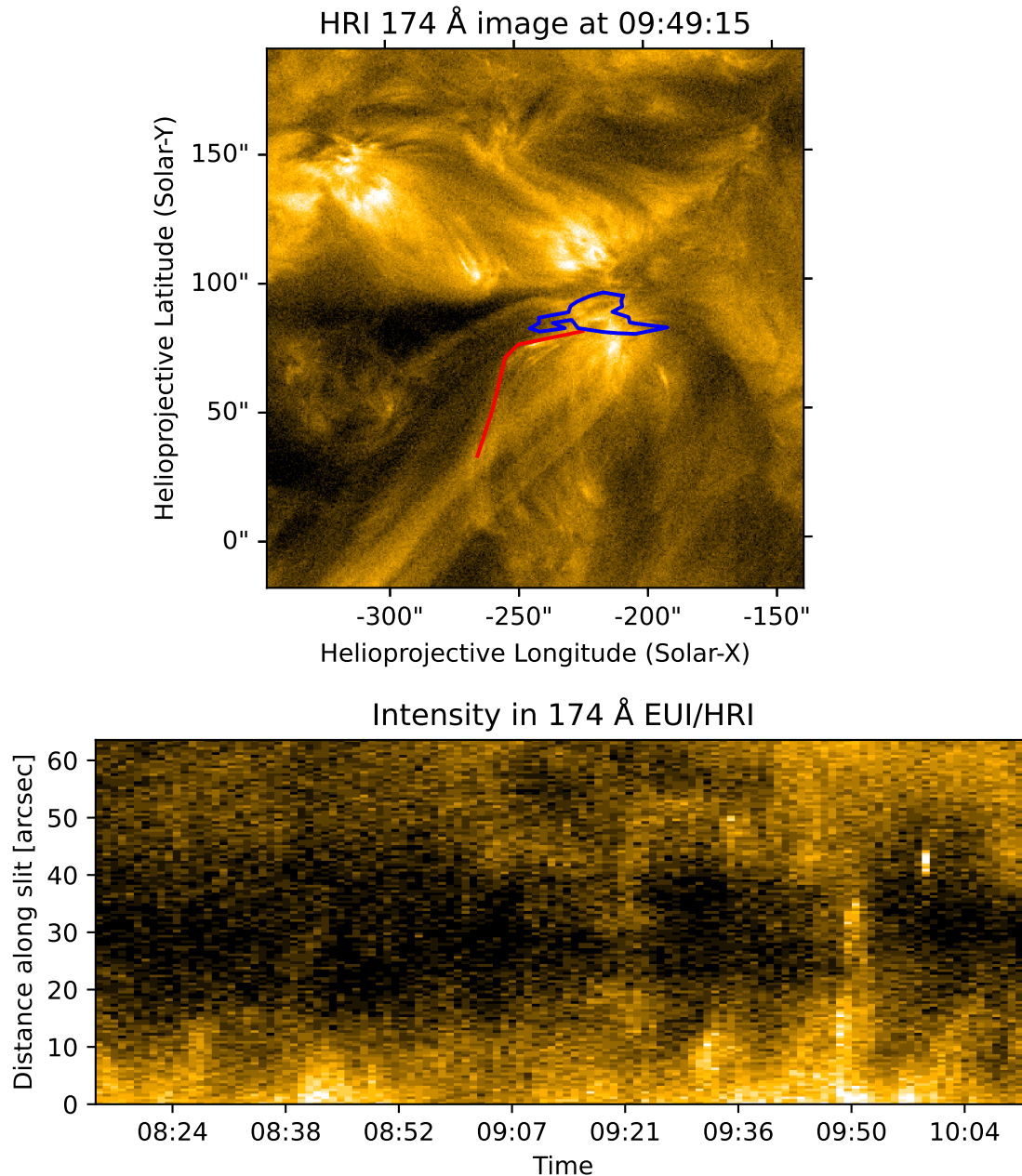


Fig. 7. Flows and brightenings measured along an artificial slit in HRI_{EUV}. Upper panel: artificial slit (red line) used to measure the intensity over time along a medium-sized active loop to the south. Lower panel: intensity vs. time plot showing various types of activity along the loop. Brightenings that propagate along the loop are seen at 08:38 and 09:44 UT. Furthermore, a localised, non-propagating brightening is present at 09:56 UT.

However, the slit of Hinode/EIS does not cross it. The mini-filament eruption is seen much more faintly in HRI_{EUV} than in SDO/AIA since the latter has a waveband that is more sensitive to cooler temperatures. Its exact eruption time cannot be determined from HRI_{EUV}, but taking the given range from SDO/AIA 10:10 to 10:15 UT, this falls exactly into the time, where the first EUV brightening from 10:08 to 10:13 UT has disappeared and the second one from 10:17 to 10:37 has not started yet. This span of four minutes might be the time when the mini-filament erupts. The question of how this complex chain of multiple events, occurring mostly in the south-east of the studied region, can cause extended coronal upflows with an elliptical shape towards the north-west could be understood by examining the large-scale magnetic field in its neighbourhood. We, then,

look at the synoptic map of Carrington Rotation (CR) 2255. The upper panel of Fig. 13 shows a synoptic magnetogram provided by the National Solar Observatory Global Oscillations Network Group (NSO/GONG; Harvey et al. 1996) data¹ for 17 March 2022 at 8:14:00 UT. The black circle indicates the location of the region of interest. The bottom panel of Fig. 13 shows the Potential Field Source Surface (PFSS) extrapolation, highlighting the coronal holes present at that time as well as sets of closed field lines; this is available in NSO/GONG web page². A clear extension of the southern coronal hole around the region of interest

¹ <https://gong2.nso.edu/products/scaleView/view.php?configFile=configs/quickreduce.cfg>

² <https://nso.edu/data/nisp-data/pfss/>

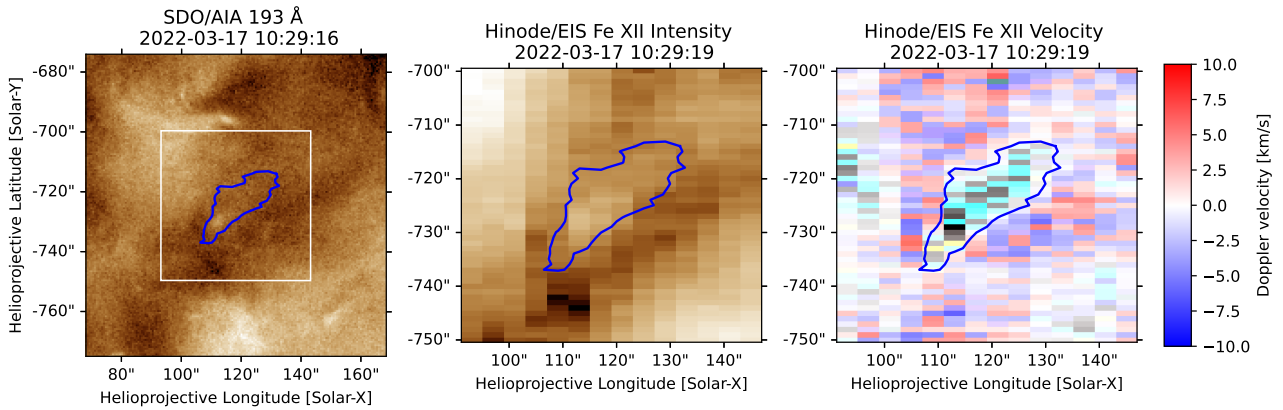


Fig. 8. Coronal emissions and Doppler shifts seen in Fe XII. Left panel: AIA 193 Å region of interest. The upflow feature is located in the quiet Sun and highlighted by a blue contour. It is located in a low-intensity region. Within that region, a small brightening can be seen at the south-eastern end at around $[115'', -730'']$. The nearby vicinity does not show any structures that are typically associated with outflows, such as obvious jets. A white box indicates the field-of-view that is used for the two other panels of this figure. Middle panel: intensity plot of the Fe XII emission line from Hinode/EIS showing a similar structure as the corresponding AIA 193 Å image, but with lower spatial resolution. The bright feature at $[115'', -728'']$ in the lower part of the Hinode/EIS image is more blurred and less intense than its vicinity in comparison to its AIA counterpart, where it is as bright as the brightest regions in the $50'' \times 50''$ field-of-view. Beneath it a small, rather dark region, is present. Right panel: derived Doppler velocities from the Fe XII emission line showing upflows, which is highlighted by the contour. The displayed blue contour is the zero-velocity line that divides regions of upflows and downflows. The strongest upflows are seen in the south-east with speeds of around -7 km s^{-1} . Most of the vicinity shows downflows or comparably weak upflows.

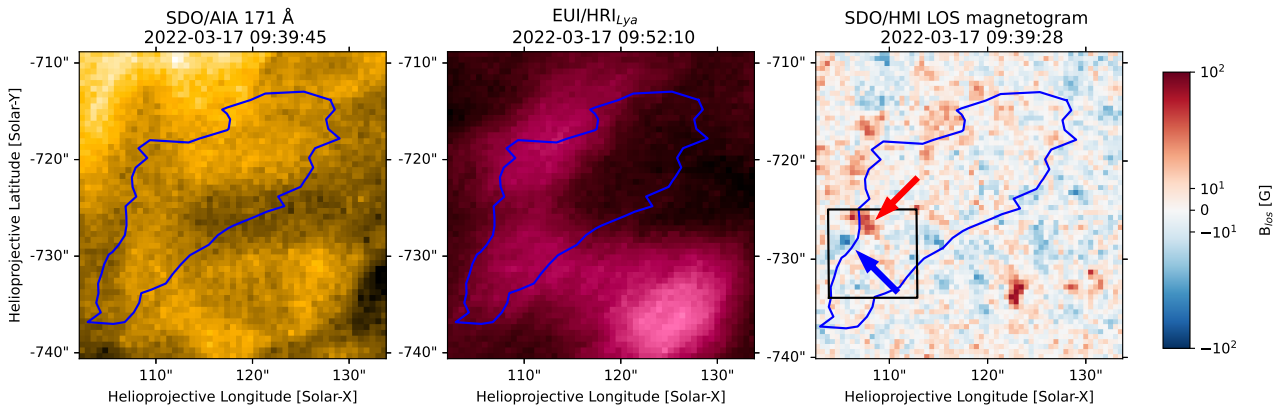


Fig. 9. Coronal emissions in Fe IX, the chromospheric network in Ly- α , and the photospheric LOS magnetic field. Left panel: SDO/AIA 171 Å image showing a strong bright feature north-east of the upflow region at $[110'', -705'']$. In the lower part between solar-X: $105\text{--}130''$ and solar-Y: -728 to $745''$ a weaker bright point is seen. The upflow region covers the eastern part of this bright point structure. Central panel: data from the HRI_{Ly α} showing that the region of the strongest upflow in the south-east is located on the chromospheric network. The upper part is located on the network boundary. Right panel: photospheric LOS magnetic field from SDO/HMI showing several smaller polarities within the upflow region, which is highlighted by the blue contour. In the lower part of the upflow, a positive polarity (red arrow) is seen with a smaller negative polarity (blue arrow). A black square indicates the region in which flux cancellation is measured for Fig. 11. The [online movie 5](#) of the HMI LOS magnetogram shows the temporal evolution.

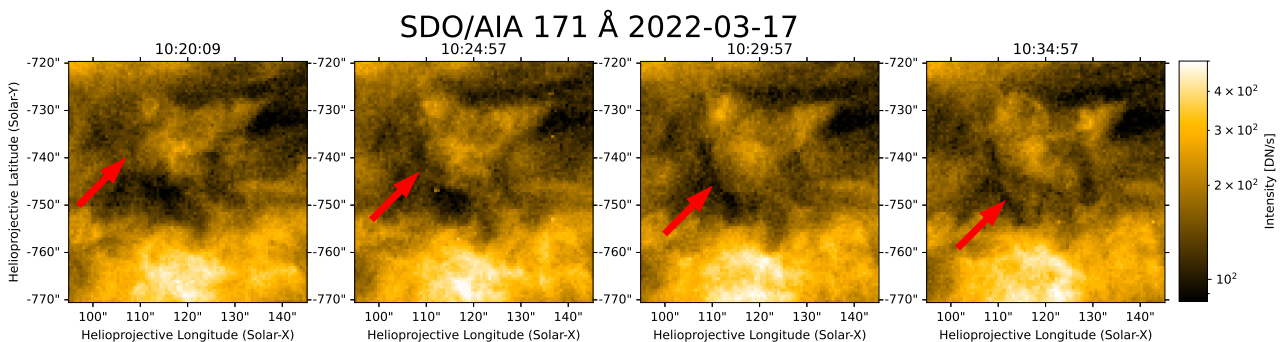


Fig. 10. Mini-filament eruption seen best in the SDO/AIA 171 Å waveband. The mini-filament erupts at $[110'', -740'']$ and then travels southwards. Its movement is highlighted by red arrows.

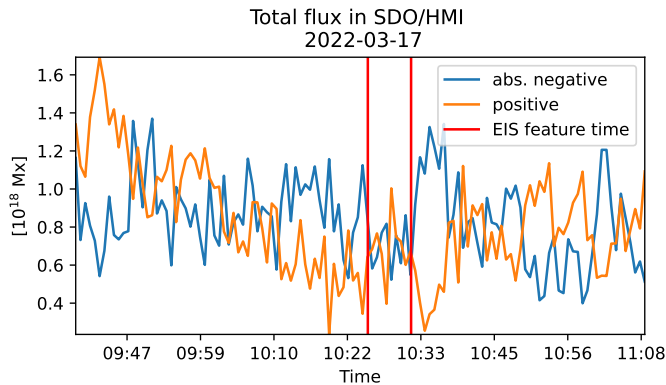


Fig. 11. Total flux within the region of the strongest upflow (highlighted by a black box in Fig. 9) starting with a strong positive and weak negative polarity at 09:40 UT. The positive flux gets cancelled out by the rising negative polarity until it exceeds it at 10:30 UT. Towards the end, no strong polarities are present. The vertical red line shows the time when the upflow was measured by Hinode/EIS.

is visible. Then, we speculate that the open field could have channelled part of the mini-filament plasma, as well as plasma expelled during other stages of the event cascade, resulting in an extended upflowing region.

The second event can be seen as a previously unrecognised source of coronal upflow. It shows an elliptical blueshifted region with speeds of up to -7.2 km s^{-1} , but no prominent intensity enhancement in the corresponding EIS Fe XII intensity data. The imaging data from SDO/AIA does not give a complete explanation, but only reveals a blurred brightening followed by a mini-filament eruption travelling towards the opposite direction where we see the upflow in Hinode/EIS. However, when inspecting HRI_{EUV} data, a series of small, spatially distributed EUV brightenings is seen followed by a bigger, relatively complex structure. It lasts for around 20 min and changes its shape over time. A system of perpendicular loops can be seen. The driving mechanism can be better understood through SDO/HMI, where we see the cancellation of a positive polarity by an arising negative one. A complete explanation for the upflow can only be given by combining all instruments: We see a triangular-shaped structure in SDO/AIA 171 Å with a positive and weak negative polarity in SDO/HMI. Then, at the north-east top of this structure, we observe a mini-flare in SDO/AIA, which, however, is highly structured in HRI_{EUV}. This feature is probably caused by the cancellation of two opposite polarities preceded by magnetic reconnection. This then triggers a mini-filament that erupts toward the south-east accompanied by a brighter circular eruption, which restructures the magnetic loops within the triangular-shaped structure. The energy is released as further brightenings within this structure. The direction of the upflow can be explained by inspecting the global magnetic field lines for this region. This demonstrates that a small, but rather complex EUV feature can trigger a cascade of multiple events, which then act as a source of coronal upflow. In this case, the upflow is caused by the cascade of observed events, triggered by the small, complex structure in HRI_{EUV} and is among the smallest known structures to cause upflow so far.

5. Discussion and conclusions

We analysed two regions of coronal upflows observed by Hinode/EIS in the Fe XII 195.12 Å line observed at $\approx 1.5 \text{ MK}$.

The two features show upflows that are of similar strength but vary strongly in terms of size. These regions were observed simultaneously by both SDO and Solar Orbiter during its first perihelion. Although SDO/AIA images show diffuse brightenings likely associated with the upflows, they do not reveal the fine structures of the EUV features that might be the source of the upflows. The high-resolution images from HRI_{EUV} show several small-scale, highly dynamic features associated with EUV brightenings.

The first upflow region, which appeared on 08 March 2022 at around 08:36 UT is seen over a system of larger loops with lifetimes of several hours. Although the loops could be identified clearly in SDO/AIA images, the HRI_{EUV} draws a clearer picture of the plasma dynamics associated with the seemingly episodic magnetic reconnection. Loop brightenings or plasma propagation along the loops are observed, for which we measured speeds of about 33 km s^{-1} : this is about four times greater than the plasma speed measured by Hinode/EIS. They are potential sources of the observed upflow. Similar activity in loops of an AR that have upflowing plasma has been reported by Barczynski et al. (2023) in a study with a quadrature observation. They have measured Doppler velocities with Hinode/EIS in an open AR loop of about -8.6 km s^{-1} and a stable plasma flow in the intensity of HRI_{EUV} of about 9.9 km s^{-1} . While the upflow speeds are comparable to our measurements, the flows in HRI_{EUV} are lower by a factor of three. This might be due to the different viewing angles, size scales of the features, and open versus closed loops. Our loop system is rooted on one end at a dominant positive magnetic flux that coincides with the chromospheric network. Flux cancellation can be seen at the edges of the positive polarity magnetic concentration. The photospheric magnetic flux cancellation is either the cause of the magnetic reconnection or its byproduct, which together lead to the observed dynamics.

The second event observed on 17 March 2022 around 10:29 UT and described in Sect. 4, is more complex compared to the first event observed on 08 March 2022, and that is described in Sect. 3. The Hinode/EIS spectra provide an upflow with a Doppler speed of about -7.2 km s^{-1} , which is associated with magnetic cancellation as shown by SDO/HMI. This fine-scale magnetic field produced a complex feature composed primarily of two perpendicular EUV loops that lasted more than 20 min. This triggered a cascade within the whole region: First, a mini-filament lifts off with a bright circular front causing a restructuring with several brightenings in the larger vicinity. The plasma upflow then gets channelled along magnetic field lines towards the north-west. Even though we did not observe any jets, the measured Doppler flows are comparable to the upflows measured by Schwanitz et al. (2021), which were identified as faint X-ray jets by Sterling et al. (2022b).

The two presented upflow regions vary in size and intensity. However, they show several similarities. Both regions consist of coronal loops lying above opposite polarity magnetic fields. Flux emergence, flux cancellation, and reconnection are common to both regions and potentially drive the observed small-scale coronal activity. The primary manifestations of this coronal activity are the brightening of the plasma, which is likely due to heating, and flows along the loop in the form of plasma blobs. The spectroscopic data show upflows as Doppler shifts in both regions.

The observation of plasma thermodynamics at the smallest observable scales to date is significant and might provide insights into phenomena that were not accessible before. While Doppler upflows were previously usually associated with prominent features such as ARs, bright points, or coronal transients

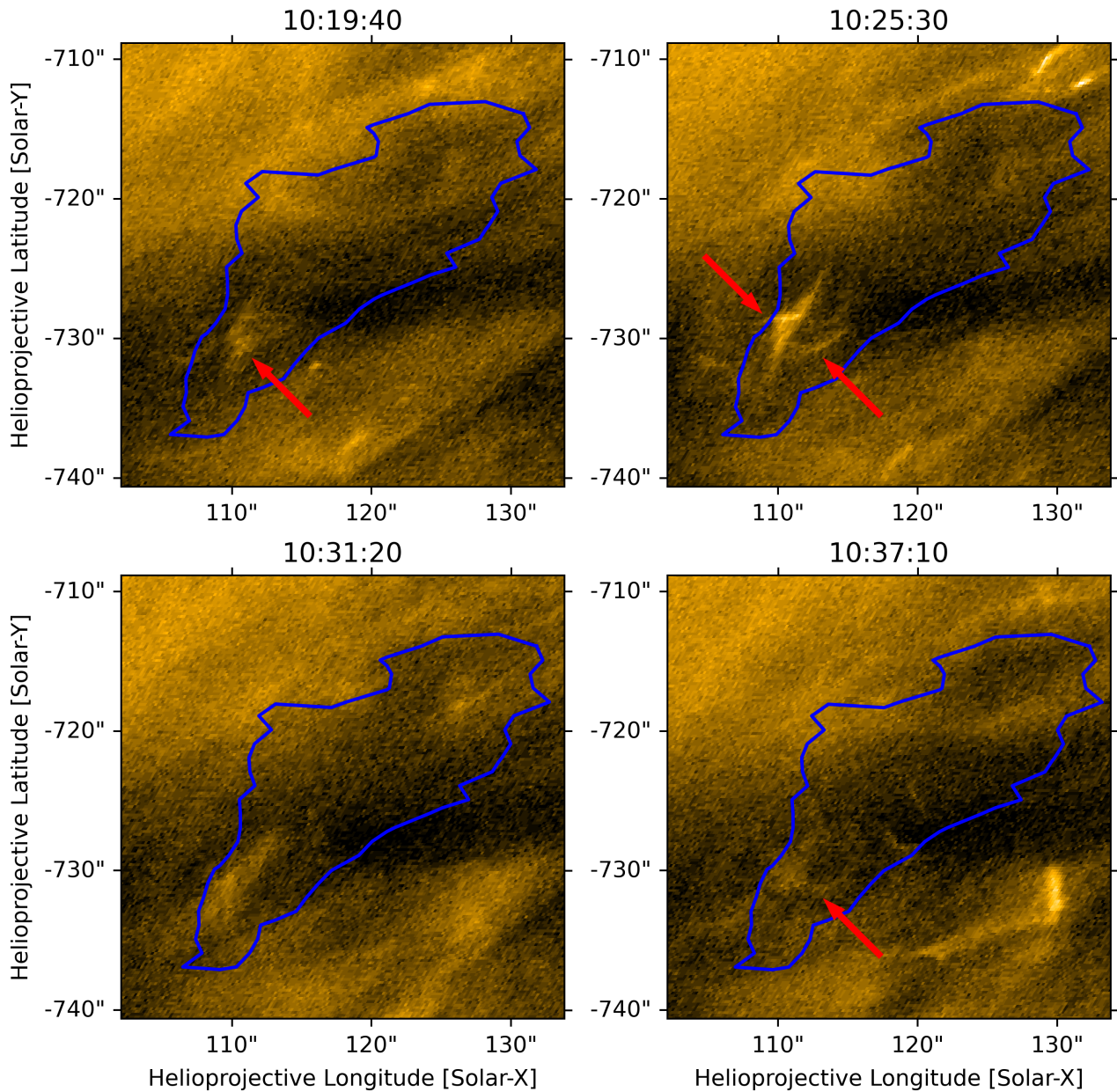
EUI/HRI_{EUV} 2022-03-17

Fig. 12. Observation with HRI_{EUV} revealing the true complexity of the event. All plots are re-projected to an Earth-based helioprojective coordinate system. Top-left panel: main EUI feature evolving as a hazy structure, where two parallel loops evolve. Top-right panel: feature becoming more complex over time. One loop becomes more prominent and starts to develop smaller, nearly perpendicular extensions (highlighted by red arrows). Two bright loops are visible in the north-west above the upflow contour. Bottom-left panel: feature starting to get fainter. Bottom-right panel: EUV feature fading away without any obvious jet. However, parts of the substructure, especially one of the perpendicular loops (highlighted by a red arrow) are still visible. Another strong brightening appears west of the upflow region.

(such as plumes and jets), the events presented here are at another level and require much higher spatial resolution and imaging cadence. The first feature is a complex loop system rooted over a strong negative polarity, where we see reoccurring brightening activity within different loop structures. This region did not show any indication of typical EUV coronal jets. The second one is a small, short-lived loop system accompanied by a mini-filament eruption, also without any obvious jets. To our knowledge, it is the smallest coronal feature in the quiet Sun for which a clear upflow has been measured. Both are loop sys-

tems but on different size scales; while the first event is probably an extension to upflows in ARs and bright points, just on much smaller scales, the second one could be an extension to upflows of mini-flares and mini-filaments.

The common properties between the two events are flux cancellation and magnetic reconnection at tiny scales. Events like the ones reported here are likely prevalent in the transition region and at the base of the solar corona. They might play a significant role in the thermal and dynamic balance of the plasma. It is plausible that we are observing some aspects of

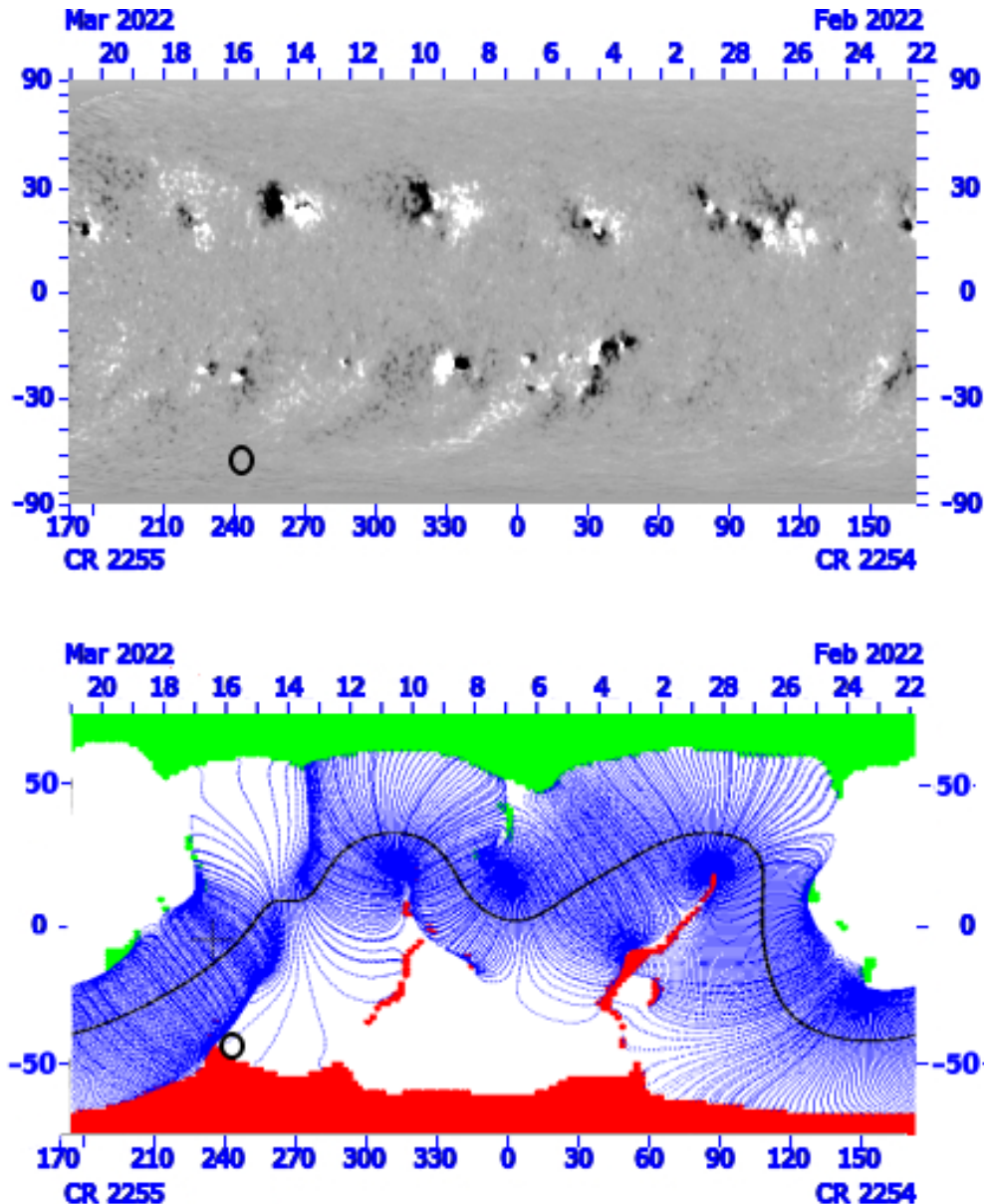


Fig. 13. Synoptic map of CR 2255 and the corresponding Potential Field Source Surface (PFSS), suggesting that the upflow region on 17 March 2022 is located in a region of open magnetic field lines. Top panel: GONG synoptic map of CR 2255. White (black) corresponds to positive (negative) polarity field; the field values have been saturated above (below) 60 G. Bottom panel: PFSS model of CR 2255. The tallest closed field lines are shown. All field lines that reach $2.5 R_{\odot}$ are open by assumption, and so the tallest closed field lines are those with a vanishing radial component just below. Such field lines separate regions of open and closed magnetic fields. Coronal holes have their footprints at the photosphere represented by patches of colour: green denotes coronal holes with positive photospheric polarity and red with negative. In the plot, the neutral line on the source surface, which shows a quasi-sinusoidal pattern, is shown by a thick black line (see <https://gong.nso.edu/data/magmap/fmodel.html>). The black circle denotes the region of interest in both panels.

the reconnection-driven nanoflares proposed by Parker (1988). We note that Raouafi et al. (2023b) proposed ubiquitous small-scale magnetic reconnection as the solar wind driver. They also argue that the magnetic reconnection occurs within open-closed field structures resulting in jetting (i.e., jetlets), and even more between closed-closed loop systems. The latter would heat and maintain the plasma at coronal temperatures.

Continued studies using the existing setup with Hinode/EIS+EUI+AIA+HMI and new data from the *Daniel K. Inouye* Solar Telescope (DKIST; Tritzschler et al. 2016) and the Polarimetric and Helioseismic Imager (PHI; Solanki et al. 2020) on

similar EIS outflow regions are necessary to better understand the observed upflows. Parts of this project were limited by the resolution of the photospheric magnetic field data from HMI; this can be overcome in the future with data from DKIST and PHI. In particular, the frequency of the loop brightenings and plasma blobs in the first event and the frequency of events comparable to the second one are of interest. We expect to see flux emergence and cancellation for many more small-scale EUV features and opposite polarities at the footpoints of small loop systems that are comparable to the events described in our paper.

Acknowledgements. C.H.M. acknowledges grants PICT-2020-SERIEA-03214, PIP 11220200100985, and UBACyT 20020170100611BA. C.H.M. is a Senior Researcher at Consejo Nacional de Investigaciones Científicas y Técnicas. A.C.S. was supported with funding from NASA's Heliophysics Supporting Research (HSR) Program, and through the NASA/MSFC Hinode Project. N.E.R. is supported by Parker Solar Probe under contract NNN06AA01C. Parker Solar Probe was designed, built, and is now operated by the Johns Hopkins Applied Physics Laboratory as part of NASA's Living with a Star (LWS) program (contract NNN06AA01C). Support from the LWS management and technical team has played a critical role in the success of the Parker Solar Probe mission. D.M.L. is grateful to the Science Technology and Facilities Council for the award of an Ernest Rutherford Fellowship (ST/R003246/1). S.P. acknowledges the funding by CNES through the MEDOC data and operations center. The ROB co-authors thank the Belgian Federal Science Policy Office (BELSPO) for the provision of financial support in the framework of the PRODEX Programme of the European Space Agency (ESA) under contract numbers 4000112292, 4000134088, 4000134474, and 4000136424. Solar Orbiter is a space mission of international collaboration between ESA and NASA, operated by ESA. The EUJ instrument was built by CSL, IAS, MPS, MSSL/UCL, PMOD/WRC, ROB, LCF/IO with funding from the Belgian Federal Science Policy Office (BELSPO/PRODEX PEA C4000134088); the Centre National d'Études Spatiales (CNES); the UK Space Agency (UKSA); the Bundesministerium für Wirtschaft und Energie (BMWi) through the Deutsches Zentrum für Luft- und Raumfahrt (DLR); and the Swiss Space Office (SSO). Hinode is a Japanese mission developed and launched by ISAS/JAXA, collaborating with NAOJ as a domestic partner, NASA and UKSA as international partners. Scientific operation of the Hinode mission is conducted by the Hinode science team organized at ISAS/JAXA. This team mainly consists of scientists from institutes in the partner countries. Support for the post-launch operation is provided by JAXA and NAOJ (Japan), UKSA (UK), NASA, ESA, and NSC (Norway). We acknowledge the use of AIA data. AIA is an instrument onboard SDO, a mission of NASA's Living With a Star program. IRIS is a NASA small explorer mission developed and operated by LMSAL with mission operations executed at NASA Ames Research Center and major contributions to downlink communications funded by ESA and the Norwegian Space Centre.

References

- Antolin, P., Pagano, P., Testa, P., Petralia, A., & Reale, F. 2021, *Nat. Astron.*, **5**, 54
- Bale, S., Badman, S., Bonnell, J., et al. 2019, *Nature*, **576**, 237
- Bale, S., Horbury, T., Velli, M., et al. 2021, *ApJ*, **923**, 174
- Barczynski, K., Harra, L., Schwanitz, C., et al. 2023, *A&A*, **673**, A74
- Berghmans, D., Clette, F., & Moses, D. 1998, *A&A*, **336**, 1039
- Berghmans, D., Auchère, F., Long, D., et al. 2021, *A&A*, **656**, L4
- Berghmans, D., Antolin, P., Auchère, F., et al. 2023, *A&A*, in press, <https://doi.org/10.1051/0004-6361/202245586>
- Chen, Y., Przybylski, D., Peter, H., et al. 2021, *A&A*, **656**, L7
- Culhane, J., Harra, L., James, A., et al. 2007, *Sol. Phys.*, **243**, 19
- Del Zanna, G. 2008, *A&A*, **481**, L49
- De Pontieu, B., Lemen, J., Kushner, G., et al. 2014, *Sol. Phys.*, **289**, 2733
- Emslie, A. G., & Noyes, R. W. 1978, *Sol. Phys.*, **57**, 373
- Fargette, N., Lavraud, B., Rouillard, A. P., et al. 2021, *ApJ*, **919**, 96
- Fox, N., Velli, M., Bale, S., et al. 2016, *Space Sci. Rev.*, **204**, 7
- Gudiksen, B. V., Carlsson, M., Hansteen, V. H., et al. 2011, *A&A*, **531**, A154
- Harra, L., Brooks, D. H., Bale, S. D., et al. 2021, *A&A*, **650**, A7
- Harrison, R. A. 1997, *The First Results from SOHO* (Berlin: Springer), 467
- Harvey, J. W., Hill, F., Hubbard, R. P., et al. 1996, *Science*, **272**, 1284
- Kahil, F., Hirzberger, J., Solanki, S. K., et al. 2022, *A&A*, **660**, A143
- Kamio, S., Hara, H., Watanabe, T., et al. 2007, *PASJ*, **59**, S757
- Lemen, J. R., Akin, D. J., Boerner, P. F., et al. 2011, *The Solar Dynamics Observatory* (Berlin: Springer), 17
- Liu, Y., Hoeksema, J., Scherrer, P., et al. 2012, *Sol. Phys.*, **279**, 295
- Madjarska, M. 2011, *A&A*, **526**, A19
- Madjarska, M. S. 2019, *Liv. Rev. Sol. Phys.*, **16**, 1
- Mampaey, B., Verbeeck, F., Stegen, K., et al. 2022, *Solo/EUI Data Release*, **5**, 2022-04
- Mandal, S., Peter, H., Chitta, L. P., et al. 2021, *A&A*, **656**, L16
- Mandrini, C. H., Baker, D., Démoulin, P., et al. 2015, *ApJ*, **809**, 73
- Moore, R. L., Cirtain, J. W., Sterling, A. C., & Falconer, D. A. 2010, *ApJ*, **720**, 757
- Moore, R. L., Sterling, A. C., Falconer, D. A., & Robe, D. 2013, *ApJ*, **769**, 134
- Moreno-Insertis, F., Galsgaard, K., & Ugarte-Urra, I. 2008, *ApJ*, **673**, L211
- Müller, D., Cyr, O. S., Zouganelis, I., et al. 2020, *A&A*, **642**, A1
- Orange, N. B., Oluseyi, H. M., Chesny, D. L., et al. 2014, *Sol. Phys.*, **289**, 1557
- Panesar, N. K., Tiwari, S. K., Berghmans, D., et al. 2021, *ApJ*, **921**, L20
- Panesar, N. K., Hansteen, V. H., Tiwari, S. K., et al. 2023, *ApJ*, **943**, 24
- Parker, E. N. 1988, *ApJ*, **330**, 474
- Pérez-Suárez, D., Maclean, R., Doyle, J., & Madjarska, M. 2008, *A&A*, **492**, 575
- Pesnell, W. D., Thompson, B. J., & Chamberlin, P. 2011, *The Solar Dynamics Observatory* (Berlin: Springer), 3
- Peter, H., Tian, H., Curdt, W., et al. 2014, *Science*, **346**, 1255726
- Raouafi, N. E. 2022, *Phys. Today*, **75**, 28
- Raouafi, N. E., & Stenborg, G. 2014, *ApJ*, **787**, 118
- Raouafi, N., Patsourakos, S., Pariat, E., et al. 2016, *Space Sci. Rev.*, **201**, 1
- Raouafi, N. E., Matteini, L., Squire, J., et al. 2023a, *Space Sci. Rev.*, **219**, 8
- Raouafi, N. E., Stenborg, G., Seaton, D. B., et al. 2023b, *ApJ*, **945**, 28
- Rochus, P., Auchère, F., Berghmans, D., et al. 2020, *A&A*, **642**, A8
- Sahu, S., Joshi, B., Sterling, A. C., Mitra, P. K., & Moore, R. L. 2022, *ApJ*, **930**, 41
- Sakao, T., Kano, R., Narukage, N., et al. 2007, *Science*, **318**, 1585
- Scherrer, P. H., Schou, J., Bush, R., et al. 2012, *Solar Physics*, **275**, 207
- Schwanitz, C., Harra, L., Raouafi, N. E., et al. 2021, *Sol. Phys.*, **296**, 1
- Shibata, K., & Magara, T. 2011, *Liv. Rev. Sol. Phys.*, **8**, 1
- Shibata, K., Ishido, Y., Acton, L. W., et al. 1992, *PASJ*, **44**, L173
- Solanki, S. K., del Toro Iniesta, J., Woch, J., et al. 2020, *A&A*, **642**, A11
- Sterling, A. C., & Moore, R. L. 2020, *ApJ*, **896**, L18
- Sterling, A. C., Moore, R. L., Falconer, D. A., & Adams, M. 2015, *Nature*, **523**, 437
- Sterling, A. C., Moore, R. L., & Panesar, N. K. 2022a, *ApJ*, **927**, 127
- Sterling, A. C., Schwanitz, C., Harra, L. K., et al. 2022b, *ApJ*, **940**, 85
- Sukarmadji, A. R. C., Antolin, P., & McLaughlin, J. A. 2022, *ApJ*, **934**, 190
- Testa, P., De Pontieu, B., Martínez-Sykora, J., et al. 2013, *ApJ*, **770**, L1
- Testa, P., De Pontieu, B., Allred, J., et al. 2014, *Science*, **346**, 1255724
- Tiwari, S. K., Hansteen, V. H., De Pontieu, B., Panesar, N. K., & Berghmans, D. 2022, *ApJ*, **929**, 103
- Tritschler, A., Rimmele, T., Berukoff, S., et al. 2016, *Astron. Nachr.*, **337**, 1064
- Widing, K. 1982, *ApJ*, **258**, 835
- Young, P., Watanabe, T., Hara, H., & Mariska, J. 2009, *A&A*, **495**, 587
- Young, P. R., Tian, H., Peter, H., et al. 2018, *Space Sci. Rev.*, **214**, 1
- Zhukov, A. N., Mierla, M., Auchère, F., et al. 2021, *A&A*, **656**, A35